

Elliptical galaxies: rotationally distorted, after all

R. Caimmi*

September 16, 2009

Abstract

On the basis of earlier investigations on homeoidally striated Mac Laurin spheroids and Jacobi ellipsoids (Caimmi and Marmo 2005; Caimmi 2006a, 2007), different sequences of configurations are defined and represented on the ellipticity-rotation plane, $(O\hat{e}\chi_v^2)$. The rotation parameter, χ_v^2 , is defined as the ratio, $E_{\text{rot}}/E_{\text{res}}$, of kinetic energy related to the mean tangential equatorial velocity component, $M(\overline{v_\phi})^2/2$, to kinetic energy related to tangential equatorial component velocity dispersion, $M\sigma_{\phi\phi}^2/2$, and residual motions, $M(\sigma_{ww}^2 + \sigma_{33}^2)/2$. Without loss of generality (above a threshold in ellipticity values), the analysis is restricted to systems with isotropic stress tensor, which may be considered as adjoint configurations to any assigned homeoidally striated density profile with anisotropic stress tensor, different angular momentum, and equal remaining parameters. The description of configurations on the $(O\hat{e}\chi_v^2)$ plane is extended on two respects, namely (a) from equilibrium to nonequilibrium figures, where the virial equations hold with additional kinetic energy, and (b) from real to imaginary rotation, where the effect is elongating instead of flattening, with respect to the rotation axis. An application is made to a subsample ($N = 16$) of elliptical galaxies extracted from richer samples ($N = 25$, $N = 48$) of early type galaxies investigated within the SAURON project (Cappellari et al. 2006, 2007). Sample objects

* *Astronomy Department, Padua Univ., Vicolo Osservatorio 2, I-35122 Padova, Italy*
email: roberto.caimmi@unipd.it fax: 39-049-8278212

are idealized as homeoidally striated MacLaurin spheroids and Jacobi ellipsoids, and their position on the ($O\hat{e}\chi_v^2$) plane is inferred from observations following a procedure outlined in an earlier paper (Caimmi 2009). The position of related adjoint configurations with isotropic stress tensor is also determined. With a single exception (NGC 3379), slow rotators are characterized by low ellipticities ($0 \leq \hat{e} < 0.2$), low anisotropy parameters ($0 \leq \delta < 0.15$), and low rotation parameters ($0 \leq \chi_v^2 < 0.15$), while fast rotators show large ellipticities ($0.2 \leq \hat{e} < 0.65$), large anisotropy parameters ($0.15 \leq \delta < 0.35$), and large rotation parameters ($0.15 \leq \chi_v^2 < 0.5$). An alternative kinematic classification with respect to earlier attempts (Emsellem et al. 2007) needs richer samples for providing additional support to the above mentioned results. A possible interpretation of slow rotators as non-rotating at all and elongated due to negative anisotropy parameters, instead of flattened due to positive anisotropy parameters, is exploited. Finally, the elliptical side of the Hubble morphological sequence is interpreted as a sequence of equilibrium (adjoint) configurations where the ellipticity is an increasing function of the rotation parameter, slow rotators correspond to early classes (E0-E2 in the oblate limit and E-2-E0 in the prolate limit) and fast rotators to late classes (E3-E6). In this view, boundaries are rotationally distorted regardless of angular momentum and stress tensor, where rotation has to be intended as due to additional kinetic energy of tangential equatorial velocity components, with respect to spherical configurations with isotropic stress tensor.

keywords - galaxies: kinematics and dynamics - galaxies: elliptical.

1 Introduction

According to their original classification (Hubble 1926), elliptical galaxies are subdivided into eight classes, designated E0, E1, ..., E7, the numerical index being the integer nearest to $10\hat{e}$, where \hat{e} is the ellipticity of related galaxies as projected on the sky, and $0 \leq \hat{e} \leq 0.7$ is inferred from observations¹. Hubble's original scheme has generally been considered satisfactory, but the physical explanation of the distorted boundary has been changed in time.

The classical interpretation starts from the evidence that (i) all celestial bodies are known to be in rotation, and (ii) the symmetry of figure shown by elliptical galaxies is precisely such as rotation might be expected to produce;

¹ In modern classifications, galaxies within the class E7 are considered as lenticulars instead of ellipticals (for further details refer to e.g., Caimmi 2006b), but it is irrelevant to the aim of the current investigation. For this reason, Hubble's original classification shall be considered in the following.

which, in turn, suggests (iii) an inquiry as to how far the observed figures of elliptical galaxies can be explained as the figures assumed by masses rotating under their own gravitation. In this view, boundaries are distorted by systematic rotation around the minor axis i.e. angular momentum parallel to the rotation axis. For further details refer to the parent textbook (Jeans 1929, Chap. XIII, §§299-302) and to recent attempts (e.g., Caimmi 2006b).

About forty years ago, observations begun to yield increasing evidence that (giant) elliptical galaxies cannot be sustained by systematic rotation (e.g., Bertola and Capaccioli 1975; Binney 1976; Illingworth 1977, 1981; Schechter and Gunn 1979). Accordingly, (giant) elliptical galaxies were conceived as systems with triplanar symmetry and ellipsoidal boundaries set up by specific anisotropic stress tensor (Binney 1976, 1978, 1980) and a negligible contribution from angular momentum. Owing to high-resolution simulations, the same holds also for (nonbaryonic) dark matter haloes hosting galaxies and clusters of galaxies (e.g., Hoeft et al. 2004; Rasia et al. 2004; Bailin and Steinmetz 2004). In this view, boundaries are distorted by systematic rotation around the minor axis and/or anisotropic stress tensor.

It is worth mentioning that an anisotropic stress tensor does not imply orbital anisotropy and vice versa. With regard to e.g., nonrotating systems, and leaving aside instabilities, orbits could be only radial or only circular, and the shape maintain spherical or flat. On the other hand, anisotropic stress tensors yield distorted boundaries (e.g., Binney 1976, 2005, the last hereafter quoted as B05). The extent to which angular momentum and anisotropic stress tensor are effective in determining the shape of a system, may be quantified by the ratio, χ_v^2 , of kinetic energy due to figure rotation to kinetic energy due to remaining motions. It is, in turn, related to a squared velocity ratio, $(\chi_v^2)_{\text{obs}}$, inferred from observations. For assigned density profiles, the dependence of the rotation parameter on the shape may be determined using the tensor virial theorem.

In the special case of homeoidally striated ellipsoids, where the isopycnic (i.e. constant density) surfaces are similar and similarly placed (Roberts 1962), the rotation parameter, χ_v , has been explicitly expressed as a function of the ellipticity, \hat{e} , restricting to oblate shapes (Binney 1976). Configurations with assigned anisotropic stress tensor are represented on the (\hat{e}, χ_v) plane as a family of curves which branch off from the origin, $(\hat{e}, \chi_v) = (0, 0)$, and increase for increasing ellipticity. The curve related to the isotropic stress tensor makes an upper limit, while their counterparts characterized by an anisotropic stress tensor ($\sigma_{11} = \sigma_{22} > \sigma_{33}$) lie below (Binney 1976).

The tidal action from an embedding, nonbaryonic dark halo makes the shape of the embedded elliptical galaxy, closer to its own. In other words, a less flattened dark halo makes a less flattened embedded elliptical galaxy,

and vice versa. Accordingly, a family of curves depending on two parameters, namely the fractional mass, $m = M_{\text{halo}}/M_{\text{egal}}$, and the axis ratio of the dark halo (supposed to be axisymmetric), ϵ_{halo} , can fit to the data on the $(\text{O}\hat{e}\chi_v)$ plane even if the stress tensor is isotropic (Caimmi 1992).

The rotation parameter, χ_v , is independent of the density profile for homeoidally striated ellipsoids (Roberts 1962; Binney 1976) which, in general, make only a first approximation to equilibrium configurations (e.g., Vandervoort 1980b; Vandervoort and Welty 1981; Lai et al. 1993). With regard to equilibrium configurations e.g., polytropes (Vandervoort 1980a), the rotation parameter, χ_v , depends on the density profile (Caimmi 1980). Accordingly, a family of curves depending on a single parameter, namely the polytropic index, n , can fit to the data on the $(\text{O}\hat{e}\chi_v)$ plane even if the stress tensor is isotropic (Vandervoort 1980a; Caimmi 1983).

Systematic rotation and anisotropic stress tensor are effective to the same extent in flattening or elongating a spherical shape, provided imaginary rotation (around the major axis) is considered in the latter case (Caimmi 1996b, 2007, 2008; the last quoted hereafter as C07, C08, respectively). The key concept is that the distribution function is independent on the sign of tangential velocity components, and the whole set of possible configurations is characterized by an equal amount of both kinetic and potential energy (Lynden-Bell 1960, 1962; Meza 2002).

In other words, clockwise and counterclockwise tangential velocity components are indistinguishable to this respect, and no change in shape occurs for any configuration between the limiting cases: (i) equal amount of clockwise and counterclockwise tangential equatorial velocity components, which implies a null mean value; (ii) only clockwise or counterclockwise tangential equatorial velocity components, which implies a maximum or minimum (according to the sign) mean value. In particular, a single configuration exists with isotropic stress tensor, to be conceived as “adjoint” to its generic counterpart with anisotropic stress tensor. The above considerations hold above a threshold in ellipticity ($\hat{e} \geq \hat{e}_{\text{adj}}$) which, on the other hand, lies below the threshold for elliptical galaxies ($\hat{e} \geq \hat{e}_{\text{ell}} \geq \hat{e}_{\text{adj}}$). Accordingly, elliptical galaxies always admit adjoints configurations with isotropic stress tensor.

The tensor virial theorem provides a rigorous global link between angular momentum, anisotropic stress tensor and shape, but the quantities appearing therein cannot easily be deduced from observations. A classical approximation to the rotation parameter, χ_v , is $(\chi_v)_{\text{obs}} = V_{\text{max}}/\sigma_0$, where V_{max} is the peak rotation velocity and σ_0 a centrally averaged velocity dispersion, both projected on the line of sight (e.g., Illingworth 1977, 1981; Schechter and Gunn 1979). With the advent of integral-field spectroscopy (Bacon et al. 2002; de Zeeuw et al. 2002; Kelz et al. 2003) a rigorous connection can be

established between the tensor virial theorem and observations, provided the former is reformulated in terms of sky-averages. In particular, the rotation parameter inferred from the data is $(\chi_v)_{\text{obs}} = \langle \tilde{v}_{\parallel}^2 \rangle^{1/2} / \langle \tilde{\sigma}_{\parallel}^2 \rangle^{1/2}$, where \tilde{v}_{\parallel} is the mean velocity projected on the line of sight, $\tilde{\sigma}_{\parallel}^2$ is the related variance, and $\langle \tilde{v}_{\parallel}^2 \rangle$, $\langle \tilde{\sigma}_{\parallel}^2 \rangle$, are sky-averages with respect to the mass (B05).

In general, the expression of the rotation parameter depends on what is intended as rotation energy. Usually, the kinetic energy is decomposed into contributions from ordered and random motions (e.g., B05). In the current attempt, the kinetic energy shall be decomposed into contributions from cylindrical rotation, $M(\overline{v_{\phi}})^2/2$, and tangential equatorial component velocity dispersion, $M\sigma_{\phi\phi}^2/2$, plus residual motions, $M(\sigma_{ww}^2 + \sigma_{33}^2)/2$; the rotation parameter, χ_v^2 , shall be defined as the ratio of the first to the sum of the remaining two above mentioned terms.

In this view, an extension to nonequilibrium configurations and imaginary rotation appears quite natural, in the light of a general theory where boudaries are distorted by angular momentum and/or anisotropic stress tensor (C07, C08) and triaxial configurations due to the occurrence of bifurcation points are also considered (Caimmi 1996a,b, 2006a,b; CM05). In dealing with imaginary tangential equatorial velocity components, the rotation parameter, χ_v^2 , has to be used instead of χ_v , where positive and negative values are related to real and imaginary angular momentum, respectively.

The present investigation is mainly devoted to the following points: (i) representation of nonequilibrium figures on the $(O\hat{e}\chi_v^2)$ plane, restricted to homeoidally striated MacLaurin spheroids and Jacobi ellipsoids and edge-on orientations with the major axis perpendicular to the line of sight; (ii) location on the $(O\hat{e}\chi_v^2)$ plane of elliptical galaxies with assigned inclination angle and anisotropy parameter, restricted to axisymmetric shapes and classified as fast and slow rotators (Cappellari et al. 2007; hereafter quoted as SX); (iii) extent to which nonequilibrium figures fit to elliptical galaxies; (iv) interpretation of slow rotators as intrinsically prolate, nonrotating bodies, and related location on the $(O\hat{e}\chi_v^2)$ plane; (v) representation of adjoint configurations in imaginary rotation with isotropic stress tensor.

The work is organized as follows. The rotation parameter, χ_v^2 , is expressed as a function of the intrinsic meridional ellipticity, \hat{e} , for equilibrium and nonequilibrium figures with isotropic stress tensor, in Section 2. The position of elliptical galaxies on the $(O\hat{e}\chi_v^2)$ plane, with regard to a restricted sample for which fiducial values of the inclination angle and the anisotropy parameter can be assigned, together with their adjoint configurations where the stress tensor is isotropic, is determined in Section 3. A comparison with earlier attempts is made in Section 4. The possibility that slow rotators are in fact

prolate, nonrotating bodies, is exploited in Section 5, where an interpretation of the elliptical side of the Hubble sequence is also proposed. The conclusion is drawn in Section 6.

2 Nonequilibrium figures

Given a mass distribution with assigned rotation axis, x_3 , the kinetic energy is usually decomposed into contributions from ordered and random motion (e.g., B05), where the former arises from mean velocity components within any infinitesimal volume element, and the latter from related variances which appear in the expression of the stress tensor. In this view, the contribution of streaming motion to velocity dispersion (along a selected direction) is not included in the stress tensor.

A different approach shall be exploited in the current attempt. More specifically, the kinetic energy shall be conceived as the sum of two contributions: one, related to either the mass-weighted tangential equatorial velocity component, $M(\overline{v_\phi})^2/2$, or the moment-of-inertia-weighted angular velocity, $I_3(\overline{\Omega})^2/2$, and one other to the contribution of the related velocity dispersion plus the remaining velocity components, radial equatorial, $(\overline{v_w^2})$, and radial polar, $(\overline{v_3^2})$. The above contributions shall be hereafter quoted as rotation kinetic energy, E_{rot} , and residual kinetic energy, E_{res} , respectively. In this view, the contribution of streaming motion to velocity dispersion (along a selected direction) is included in the stress tensor.

It is worth mentioning that the mass-weighted tangential equatorial velocity component and the moment-of-inertia-weighted angular velocity yield different kinetic energy values (for a formal discussion refer to Appendix A). As the current investigation deals with linear velocities, only the former shall be considered here.

If the tensor virial theorem holds for only time-averaged quantities, the related mass distribution can no longer be considered in dynamical or hydrostatic equilibrium, but still in virial equilibrium (C07), which makes a special kind of nonequilibrium figures. In the following, “nonequilibrium” has to be intended as “far from dynamical or hydrostatic equilibrium but still in virial equilibrium”. For nonequilibrium figures, the tensor virial equations must be related to an adjoint configuration with equal density profile and rotation energy, but different residual-energy tensor components, $(\tilde{E}_{\text{res}})_{pp} = \zeta_{pp} E_{\text{res}}$. The result is (C07):

$$2(E_{\text{rot}})_{qq} + 2\zeta_{qq} E_{\text{res}} + (E_{\text{pot}})_{qq} = 0 \quad ; \quad q = 1, 2 \quad ; \quad (1a)$$

$$2\zeta_{33} E_{\text{res}} + (E_{\text{pot}})_{33} = 0 \quad ; \quad (1b)$$

where $(E_{\text{pot}})_{pq}$ is the potential-energy tensor and the coefficients, ζ_{pp} , may be understood as generalized anisotropy parameters (CM05, Caimmi 2006a,b; C07). The combination of Eqs. (1a) and (1b) yields:

$$2(E_{\text{rot}})_{qq} - \frac{\zeta_{qq}}{\zeta_{33}}(E_{\text{pot}})_{33} + (E_{\text{pot}})_{qq} = 0 \quad ; \quad q = 1, 2 \quad ; \quad (2a)$$

$$2E_{\text{res}} = -\frac{1}{\zeta_{33}}(E_{\text{pot}})_{33} \quad ; \quad (2b)$$

and the potential-energy tensor for homeoidally striated Jacobi ellipsoids reads (CM05):

$$(E_{\text{pot}})_{pq} = -\frac{GM^2}{a_1}\nu_{\text{sel}}(B_{\text{sel}})_{pq} \quad ; \quad p, q = 1, 2, 3 \quad ; \quad (3a)$$

$$(B_{\text{sel}})_{pq} = \delta_{pq}\epsilon_{p2}\epsilon_{p3}A_p \quad ; \quad B_{\text{sel}} = \sum_{s=1}^3 \epsilon_{s2}\epsilon_{s3}A_s \quad ; \quad (3b)$$

where δ_{pq} is the Kronecker symbol, G the constant of gravitation, ν_{sel} a profile factor (i.e. depending only on the density profile), a_p are semiaxes, $\epsilon_{pq} = a_p/a_q$ axis ratios, A_p shape factors (i.e. depending only on the axis ratios).

The substitution of Eqs. (3), (42), (43), into (2) yields after some algebra:

$$(\overline{v_\phi})^2 = \frac{GM}{a_1}\nu_{\text{sel}} \left[B_{\text{sel}} - \frac{\zeta}{\zeta_{33}}(B_{\text{sel}})_{33} \right] \quad ; \quad (4a)$$

$$\sigma_{\phi\phi}^2 + \sigma_{ww}^2 + \sigma_{33}^2 = \frac{GM}{a_1}\nu_{\text{sel}} \frac{1}{\zeta_{33}}(B_{\text{sel}})_{33} \quad ; \quad (4b)$$

$$\zeta = \zeta_{11} + \zeta_{22} + \zeta_{33} \quad ; \quad (4c)$$

$$\frac{\zeta}{\zeta_{pp}} = \frac{\tilde{E}_{\text{res}}/E_{\text{res}}}{(\tilde{E}_{\text{res}})_{pp}/E_{\text{res}}} = \frac{1}{\tilde{\zeta}_{pp}} \quad ; \quad (4d)$$

$$\tilde{\zeta}_{pp} = \frac{(\tilde{E}_{\text{res}})_{pp}}{\tilde{E}_{\text{res}}} \quad ; \quad (4e)$$

where the anisotropy parameters, $\tilde{\zeta}_{pp}$, are related to equilibrium figures (CM05; C07; C08).

The rotation parameter, $\chi_v^2 = E_{\text{rot}}/E_{\text{res}}$, by use of Eqs. (4) and (43) takes the explicit expression:

$$\chi_v^2 = \frac{(\overline{v_\phi})^2}{\sigma^2} = \zeta \left[\tilde{\zeta}_{33} \frac{B_{\text{sel}}}{(B_{\text{sel}})_{33}} - 1 \right] \quad ; \quad (5a)$$

$$\sigma^2 = \sigma_{\phi\phi}^2 + \sigma_{ww}^2 + \sigma_{33}^2 = \sigma_{11}^2 + \sigma_{22}^2 + \sigma_{33}^2 \quad ; \quad (5b)$$

which, for assigned values of the anisotropy parameters, depends only on the axis ratios. In an earlier attempt (CM05) a different definition of rotation parameter has been used, in terms of a mean squared velocity, $\langle v_{\text{rot}}^2 \rangle$, instead of related squared mean velocity, $\langle v_{\text{rot}} \rangle^2$, which implies different anisotropy parameters for equal shapes and rotation parameters, in the two formulations. The current definition is more strictly connected with observations i.e. mean velocities and velocity dispersions. The factor within brackets in Eq. (5a) corresponds to equilibrium figures ($\zeta = 1, \zeta_{pp} = \tilde{\zeta}_{pp}$) while the virial index, $\zeta = \tilde{E}_{\text{res}}/E_{\text{res}}$, is a measure of the departure from equilibrium ($0 \leq \zeta < +\infty$).

For homeoidally striated Jacobi ellipsoids, the anisotropy parameters, ζ_{11} , ζ_{22} , are related to the diagonal components of the moment-of-inertia tensor, I_{11} , I_{22} , and a necessary and sufficient condition for the stress tensor to be isotropic, is $\zeta_{33} = 1/3$. In addition, bifurcation points are independent of the angular momentum and the stress tensor, and may be related to the adjoint configuration where the squared angular momentum attains a maximum or minimum value (according to the sign) and the stress tensor is isotropic. This is why the effect of an anisotropic stress tensor is equivalent to an additional real or imaginary rotation, inducing flattening (on the equatorial plane) or elongation (on the rotation axis), respectively. For further details refer to the parent paper (C07) and Appendix B. More specifically, real or imaginary rotation take place when the factor within brackets in Eq. (5a) is positive or negative, respectively.

Given a nonequilibrium figure with assigned anisotropy parameters, ζ_{pp} , the particularization of Eq. (5a) to the adjoint configuration with isotropic stress tensor ($\tilde{\zeta}_{33} = 1/3$) yields:

$$(\chi_v^2)_{\text{iso}} = \zeta \left[\frac{1}{3} \frac{B_{\text{sel}}}{(B_{\text{sel}})_{33}} - 1 \right] ; \quad (6)$$

which can be plotted as a function of the meridional ellipticity, $\hat{e} = 1 - \epsilon_{31}$, where $\hat{e} > 0$ implies real rotation, $\hat{e} = 0$ no rotation, and $\hat{e} < 0$ imaginary rotation. Cases within the range, $1/2 \leq \zeta \leq 2$, are plotted in Fig. 1, where the full curve corresponds to equilibrium figures ($\zeta = 1$) and the upper on the first quadrant ($\zeta = 1.1, 1.2, \dots, 2.0$) and the lower on the first quadrant ($\zeta = 1/1.1, 1/1.2, \dots, 1/2.0$) dotted curves to nonequilibrium figures. Points lying on the first and the third quadrant represent systems in real and imaginary rotation, respectively. The origin is the locus of nonrotating systems. The loci of different bifurcation points are represented by different vertical lines, namely: from axisymmetric to triaxial configurations (dotted); from triaxial (left) and axisymmetric (right) to pear-shaped configurations (dashed); and,

in addition: onset of dynamical instability in axisymmetric configurations (dot-dashed). The first and the third quadrant can completely be filled with curves expressed by Eq. (6), where the limiting case, $\zeta = 0$, corresponds to flat configurations with no centrifugal support, and the limiting case, $\zeta \rightarrow +\infty$, corresponds to nonflat configurations with no pressure support.

In the general case of anisotropic stress tensor, conformly to Eq. (5a), the trend on the $(O\hat{e}\chi_v^2)$ plane is similar but the curves are shifted on the right (nonrotating flattened configurations) or on the left (nonrotating elongated configurations), according if $\sigma_{11}^2 = \sigma_{22}^2 > \sigma_{33}^2$ or $\sigma_{11}^2 = \sigma_{22}^2 < \sigma_{33}^2$, respectively. In any case, the adjoint equilibrium configurations with isotropic stress tensor lie on the related sequence (full curve in Fig. 1) with unchanged axes, which implies a vertical shift of a selected point on the $(O\hat{e}\chi_v^2)$ plane, until the adjoint configuration is attained.

3 Comparison with observations

Aiming in comparing model predictions to data from observations, the position of elliptical galaxies on the $(O\hat{e}\chi_v^2)$ plane shall be determined. The sample used (Caimmi and Valentinuzzi 2008; Caimmi 2009b; hereafter quoted as CV08 and C09, respectively) is extracted from richer samples of early-type galaxies investigated within the SAURON project (SIV, SX). The following parameters may directly be deduced or derived from observations: the effective (half-light) radius, R_e ; the stellar mass within the effective radius, $M_e = M(R_e) = M/2$; the luminosity-weighted average ellipticity, on a plane perpendicular to the line of sight, $\langle \hat{e}_\perp \rangle$, within either an isophote enclosing an area, $\hat{A} = \pi R_e^2$, or the largest isophote fully contained within the SAURON field, whichever is smaller; the luminosity-weighted squared mean velocity component, parallel to the line of sight, $\langle \tilde{v}_\parallel^2 \rangle$, within either an ellipse of area, \hat{A} , ellipticity, \hat{e}_\perp , and related position angle, or the largest similar ellipse fully contained within the SAURON field, whichever is smaller; the luminosity-weighted squared velocity dispersion, parallel to the line of sight, $\langle \sigma_\parallel^2 \rangle$, within either an ellipse of area, \hat{A} , ellipticity, \hat{e}_\perp , and related position angle, or the largest similar ellipse fully contained within the SAURON field, whichever is smaller. For further details refer to the parent papers (SIV; SX) and an earlier attempt (B05).

Two additional parameters can be inferred by fitting the data with dynamic models. More specifically, the inclination angle, i , is deduced from the best fitting two-integral Jeans model (SIV), and the anisotropy parameter, δ , is determined from the solution of the dynamic models, supposed to be axisymmetric (SX). It is worth remembering that fast rotators show

evidence of large anisotropy and axial symmetry, while slow rotators appear to be nearly isotropic and moderately triaxial (SX).

The anisotropy parameter (e.g., B05):

$$\delta = 1 - \frac{\sigma_{33}^2}{\sigma_{11}^2} = 1 - \frac{\sigma_{33}^2}{\sigma_{22}^2} ; \quad (7a)$$

$$\sigma_{11} = \sigma_{22} \geq \sigma_{33} ; \quad (7b)$$

may be related to the generalized anisotropy parameters, ζ_{pp} , via Eqs. (4d), (4e), in the special case of equilibrium figures, as:

$$\delta = 1 - \frac{\zeta_{33}}{\zeta_{11}} = 1 - \frac{\zeta_{33}}{\zeta_{22}} = \frac{1 - 3\zeta_{33}}{1 - \zeta_{33}} = \frac{3\zeta_{11} - 1}{\zeta_{11}} = \frac{3\zeta_{22} - 1}{\zeta_{22}} ; \quad (8)$$

which is restricted to homeoidally striated MacLaurin spheroids.

For representing sample objects on the $(\mathbf{O}\hat{e}\chi_v^2)$ plane, intrinsic values of velocities and ellipticities with regard to edge-on configurations have to be used, instead of projected values along the line of sight. The corrections for edge-on (edo) configurations are (Binney and Tremaine 1987, Chap. 4, §4.3):

$$1 - \epsilon_{31}^2 = \frac{1 - \langle \epsilon_{\perp} \rangle^2}{\sin^2 i} ; \quad (9)$$

$$\hat{e} = 1 - \epsilon_{31} = 1 - \left[1 - \frac{1 - \langle \hat{e}_{\perp} \rangle (2 - \langle \hat{e}_{\perp} \rangle)}{\sin^2 i} \right]^{1/2} ; \quad (10)$$

for the meridional axis ratio and ellipticity, where $\langle \epsilon_{\perp} \rangle$ and $\langle \hat{e}_{\perp} \rangle$ are the luminosity averaged axis ratio and ellipticity related to an inclination angle, i , between the symmetry axis and the line of sight ($i = 90^\circ$ for edge-on configurations), and:

$$[\langle \tilde{v}_{\parallel}^2 \rangle]_{\text{edo}} = \frac{[\langle \tilde{v}_{\parallel}^2 \rangle]_{\text{obs}}}{\sin^2 i} ; \quad (11)$$

$$[\langle \sigma_{\parallel}^2 \rangle]_{\text{edo}} = \frac{[\langle \sigma_{\parallel}^2 \rangle]_{\text{obs}}}{1 - \delta \cos^2 i} ; \quad (12)$$

under the assumption of axisymmetric ($a_1 = a_2$) configurations with axisymmetric ($\sigma_{11} = \sigma_{22}$) stress tensor (SX).

The intrinsic squared mean rotational velocity and squared velocity dispersion are:

$$(\overline{v_{\phi}})^2 = 2[\langle \tilde{v}_{\parallel}^2 \rangle]_{\text{edo}} ; \quad (13)$$

$$\begin{aligned} \sigma^2 &= \sigma_{11}^2 + \sigma_{22}^2 + \sigma_{33}^2 = 2[\langle \sigma_{\parallel}^2 \rangle]_{\text{edo}} + (1 - \delta)[\langle \sigma_{\parallel}^2 \rangle]_{\text{edo}} \\ &= (3 - \delta)[\langle \sigma_{\parallel}^2 \rangle]_{\text{edo}} ; \end{aligned} \quad (14)$$

in terms of edge-on mean rotational velocity and velocity dispersion, and:

$$(\overline{v_\phi})^2 = \frac{2}{\sin^2 i} [< \tilde{v}_\parallel^2 >]_{\text{obs}} ; \quad (15)$$

$$\sigma^2 = \frac{3 - \delta}{1 - \delta \cos^2 i} [< \sigma_\parallel^2 >]_{\text{obs}} ; \quad (16)$$

in terms of observed mean rotational velocity and velocity dispersion.

The intrinsic rotation parameter, by use of Eqs. (14), (15), (16) and (45), reads:

$$(\chi_v^2)_{\text{int}} = \frac{(\overline{v_\phi})^2}{\sigma^2} = \frac{2}{\sin^2 i} \frac{1 - \delta \cos^2 i}{3 - \delta} \frac{[< \tilde{v}_\parallel^2 >]_{\text{obs}}}{[< \sigma_\parallel^2 >]_{\text{obs}}} ; \quad (17)$$

and sample objects may be represented on the $(\text{O}\hat{e}\chi_v^2)$ plane using Eqs. (10) and (17).

The dimensionless energy:

$$\kappa = \frac{\sigma_{11}^2 a_1}{GM} ; \quad (18)$$

may be considered as the extent to which gravitation is balanced by centrifugal forces at the top major axis, a_1 , as $-F_C/F_G \approx \kappa$. With regard to $[\text{M}_{10} \text{ kpc Gyr}]$ units, $\text{M}_{10} = 10^{10} \text{m}_\odot$, the constant of gravitation is $G = 4.493 \cdot 10^4 \text{M}_{10}^{-1} \text{kpc}^3 \text{Gyr}^{-2}$ and assuming as typical values $M = 10^2 \text{M}_{10}$, $a_1 = 10 \text{kpc}$, $\sigma_{11}^2 = 4.493 \cdot 10^4 \text{kpc Gyr}^{-1}$, Eq. (18) yields $\kappa = 0.1$ as expected for elliptical galaxies. On the other hand, observed quantities are related to the effective radius, R_e , instead of the major semiaxis, a_1 , and the dimensionless energy has to be approximated as:

$$\kappa_{\text{edo}} = \frac{[< \sigma_\parallel^2 >]_{\text{edo}} R_e}{GM_e} ; \quad (19)$$

in connection with edge-on configurations.

For the sample of elliptical galaxies under consideration ($N = 16$), the values of the following parameters are listed in Tab. 1: the effective (half-light) radius, R_e (CV08); the intrinsic mean equatorial tangential velocity component, $\overline{v_\phi}$, Eq. (15); the intrinsic velocity dispersion, σ , Eq. (16); the galaxy stellar mass within the effective radius, $M_e = M(R_e) = M/2$, under the assumption that luminosity traces the mass (CV08); the dimensionless energy, κ_{edo} , Eq. (19); the inclination angle, i , of the best fitting two-integral Jeans model (SIV); the anisotropy parameter, δ , determined from the solution of the dynamic models, supposed to be axisymmetric (SX); the intrinsic ellipticity, \hat{e} , deduced from the computed inclination, Eq. (10), under the assumption of axisymmetric configurations (SX); the sample object rotation

Table 1: Parameters calculated from the data related to a sample ($N = 16$) of elliptical galaxies, extracted from larger samples of early-type galaxies investigated within the SAURON project (SIV, $N = 25$; SX, $N = 48$). Values of dimensional quantities are expressed in [M_{10} kpc Gyr] units (1 kpc/Gyr=0.978 46 km/s; 1 km/s=1.022 01 kpc/Gyr), and angles in degrees. Column captions: (1) NGC number; (2) effective (half-light) radius, R_e (CV08); (3) intrinsic mean equatorial tangential velocity component, $\overline{v_\phi}$, Eq. (15); (4) intrinsic velocity dispersion, σ , Eq. (16); (5) galaxy stellar mass within the effective radius, $M_e = M(R_e) = M/2$, under the assumption that luminosity traces the mass (CV08); (6) dimensionless energy, κ_{edo} , Eq. (19); (7) inclination angle, i , of the best fitting two-integral Jeans model (SIV); (8) anisotropy parameter, δ , determined from the solution of the dynamic models, supposed to be axisymmetric (SX); (9) intrinsic ellipticity, \hat{e} , deduced from the computed inclination, Eq. (10), under the assumption of axisymmetric configurations (SX); (10) sample object rotation parameter, $(\chi_v^2)_{\text{int}}$, Eq. (17); (11) adjoint configuration rotation parameter, χ_v^2 , Eq. (6); (12) kinematic classification, where F and S denote fast and slow rotators, respectively (SX). For the original data refer to the parent papers (SIV; SX). For further details refer, in addition, to earlier attempts (B05; CV08; C09).

NGC	R_e	$\overline{v_\phi}$	σ	M_e	κ_{edo}	i	δ	\hat{e}	$(\chi_v^2)_{\text{int}}$	χ_v^2	KC
0821	4.43	069	311	10.26	0.33	90	0.20	0.40	0.05	0.35	F
2974	2.43	219	317	07.61	0.26	57	0.24	0.62	0.47	0.46	F
3377	2.01	082	198	02.35	0.27	90	0.25	0.46	0.17	0.38	F
3379	2.09	040	349	08.80	0.22	90	0.03	0.08	0.01	0.05	F
3608	4.43	012	310	09.77	0.34	90	0.13	0.18	0.00	0.12	S
4278	2.43	090	410	09.64	0.33	45	0.18	0.26	0.05	0.19	F
4374	6.15	010	492	36.35	0.31	90	0.08	0.15	0.00	0.09	S
4458	2.19	014	146	01.50	0.24	90	0.09	0.12	0.01	0.07	S
4473	2.00	062	318	07.86	0.22	73	0.34	0.46	0.04	0.38	F
4486	7.96	010	542	45.97	0.38	90	0.00	0.04	0.00	0.02	S
4552	2.32	019	453	12.62	0.28	90	0.02	0.04	0.00	0.02	S
4621	3.97	075	355	18.80	0.21	90	0.18	0.34	0.04	0.27	F
4660	0.67	122	279	02.11	0.20	70	0.30	0.53	0.19	0.40	F
5813	7.90	046	389	28.89	0.32	90	0.08	0.15	0.01	0.09	S
5845	0.56	117	390	03.02	0.22	90	0.15	0.35	0.09	0.29	F
5846	9.51	010	424	37.19	0.34	90	0.01	0.07	0.00	0.04	S

parameter, $(\chi_v^2)_{\text{int}}$, Eq. (17); the adjoint configuration rotation parameter, χ_v^2 , Eq. (6); together with the kinematic classification, where F and S denote fast and slow rotators, respectively (SX). For the original data refer to the parent papers (SIV; SX). For further details refer, in addition, to earlier attempts (B05; CV08; C09). It can also be seen that $\kappa_{\text{edo}} = 0.20\text{--}0.34$ for the whole sample, which implies gravitation is not balanced by centrifugal force in elliptical galaxies, as expected.

The position of fast and slow rotators on the $(O\hat{e}\chi_v^2)$ plane, is shown in Fig. 2 as squares and diamonds, respectively. Three curves are also reproduced from Fig. 1, namely equilibrium figures ($\zeta = 1$, full line) and nonequilibrium figures ($\zeta = 1.1$, up on the first quadrant; $\zeta = 0.5$, down on the first quadrant; dotted lines) with isotropic stress tensor. The caption of the vertical lines is the same as in Fig. 1. The adjoint configurations with isotropic stress tensor and equal shape, are also positioned on the sequence of equilibrium figures using the same symbols, as the result of a vertical shift. A similar procedure holds, in general, for an assigned sequence of nonequilibrium figures with isotropic stress tensor. An inspection of Fig. 2 shows the following features.

All sample objects lie below the lower sequence ($\zeta = 0.5$), with the exception of the most flattened galaxy (NGC 2974), which is placed just above the middle sequence ($\zeta = 1$).

In general, slow rotators (diamonds) are placed on the left with respect to fast rotators (squares) with a single exception (NGC 3379) which, on the other hand, shows a nearly isotropic stress tensor ($\delta = 0.03$), a nearly spherical shape ($\hat{e} = 0.04$), and a velocity ratio, $\{[< \tilde{v}_{\parallel}^2 >]_{\text{obs}}/[< \sigma_{\parallel}^2 >]_{\text{obs}}\}^{1/2} = 0.14$, equal to the maximum value found in slow rotators (NGC 5813). A similar trend is exhibited by adjoint configurations with isotropic stress tensor, which are vertically shifted on the sequence of equilibrium figures, full line in Fig. 2.

If slow rotators (including NGC 3379) are assumed to be nonrotating ($\overline{v_{\phi}} = 0$) within the observational errors and elongated ($\hat{e} < 0$) due to an anisotropic stress tensor ($\sigma_{11} = \sigma_{22} < \sigma_{33}$ or $\delta < 0$), the related adjoint configurations with isotropic stress tensor are elongated due to imaginary rotation, conformly to Eq. (6). More specifically, the major axis coincides with the polar axis and the meridional axis ratio exceeds unity, yielding a negative ellipticity, $\hat{e} = 1 - \epsilon_{31} < 0$, which produces, in turn, a negative anisotropy parameter, $\delta = 1 - \sigma_{33}^2/\sigma_{11}^2 < 0$, by generalizing Eq. (7a) to the case under discussion, $\sigma_{11} = \sigma_{22} < \sigma_{33}$.

In this view, let \hat{e}_{fa} , δ_{fa} , be the intrinsic ellipticity from Eq. (10) and the anisotropy parameter determined by comparison with the dynamic models, for axisymmetric flattened configurations (SX), and \hat{e}_{elo} , δ_{elo} , their counter-

Table 2: The intrinsic ellipticity, \hat{e} , the anisotropy parameter, δ , and the square root of the absolute value of the rotation parameter, $|\chi_v^2|^{1/2}$, for slow rotators (NGC 3379 included) supposed to be flattened (fla) as in Tab. 1, or elongated (elo) with equal major axis, according to Eqs. (20) and (21). The square root of the absolute value of the rotation parameter has been listed for better appreciating the difference between flattened and elongated configurations.

NGC	\hat{e}_{fla}	δ_{fla}	$ (\chi_v^2)_{\text{fla}} ^{1/2}$	$-\hat{e}_{\text{elo}}$	$-\delta_{\text{elo}}$	$ (\chi_v^2)_{\text{elo}} ^{1/2}$
3379	0.08	0.03	0.22	0.09	0.03	0.21
3608	0.18	0.13	0.34	0.22	0.15	0.31
4374	0.15	0.08	0.31	0.18	0.09	0.28
4458	0.12	0.09	0.27	0.14	0.10	0.25
4486	0.04	0.00	0.15	0.04	0.00	0.15
4552	0.04	0.02	0.15	0.04	0.02	0.15
5813	0.15	0.08	0.31	0.18	0.09	0.28
5846	0.07	0.01	0.20	0.08	0.01	0.19

parts related to equal values of intrinsic axes and stress tensor components, but with the major axis related to the symmetry axis instead of the equatorial plane. Accordingly, the following changes must be performed: $\epsilon_{31} \rightarrow \epsilon_{31}^{-1}$; $\sigma_{33} \rightarrow \sigma_{11}$; $\sigma_{11} \rightarrow \sigma_{33}$; which, using Eqs. (7) and (10), yields:

$$\hat{e}_{\text{elo}} = 1 - \epsilon_{31}^{-1} = 1 - (1 - \hat{e}_{\text{fla}})^{-1} = \frac{-\hat{e}_{\text{fla}}}{1 - \hat{e}_{\text{fla}}} ; \quad (20)$$

$$\delta_{\text{elo}} = 1 - \left(\frac{\sigma_{33}}{\sigma_{11}} \right)^{-2} = 1 - (1 - \delta_{\text{fla}})^{-1} = \frac{-\delta_{\text{fla}}}{1 - \delta_{\text{fla}}} ; \quad (21)$$

where the values related to flattened configurations are listed in Tab. 1 and again in Tab. 2 for slow rotators (NGC 3379 included), together with their counterparts related to elongated configurations and, in both cases, the values of the rotation parameter, χ_v , for adjoint configuration with isotropic stress tensor. The square root of the rotation parameter has been listed for better appreciating the difference between flattened and elongated configurations.

The position of slow rotators (NGC 3379 included) on the ($\text{O}\hat{e}\chi_v^2$) plane in the case under discussion, is indicated in Fig. 3 as diamonds and a single square, while nothing changes for the remaining fast rotators (squares) and captions, with respect to Fig. 2.

4 Comparison with earlier attempts

For equilibrium figures ($\zeta = 1$) viewed edge-on ($i = 90^\circ$), the combination of Eqs. (3), (5), (8), and (17) yields:

$$(\chi_v^2)_C = \frac{[\langle \tilde{v}_{\parallel}^2 \rangle]_{\text{edo}}}{[\langle \sigma_{\parallel}^2 \rangle]_{\text{edo}}} = (1 - \delta) \frac{(B_{\text{sel}})_{11}}{(B_{\text{sel}})_{33}} - 1 ; \quad (22)$$

which is formally coincident with classical results, where $\langle \tilde{v}_{\parallel}^2 \rangle$ and $\langle \sigma_{\parallel}^2 \rangle$ are intended as a mass-averaged, one-dimension squared rotation velocity and related variance, respectively (e.g., B05).

If, on the other hand, $\langle \tilde{v}_{\parallel}^2 \rangle$ and $\langle \sigma_{\parallel}^2 \rangle$ are conceived as sky-averages, according to the current notation, and the kinetic energy is decomposed into contributions from ordered and random motions, the right-hand side of Eq. (22) has to be divided by a correction factor. The result is (B05):

$$(\chi_v^2)_B = \frac{[\langle \tilde{v}_{\parallel}^2 \rangle]_{\text{edo}}}{[\langle \sigma_{\parallel}^2 \rangle]_{\text{edo}}} = \frac{(1 - \delta)(B_{\text{sel}})_{11}/(B_{\text{sel}})_{33} - 1}{\psi(1 - \delta)(B_{\text{sel}})_{11}/(B_{\text{sel}})_{33} + 1} ; \quad (23)$$

where ψ is an integral which depends on the density profile and the rotation curve of the matter distribution.

In the present investigation, Eq. (22) holds provided the kinetic energy is decomposed into contributions from cylindrical rotation and residual motions, which implies a different anisotropy parameter with respect to Eq. (23). The left-hand sides of Eqs. (22) and (23):

$$(\chi_v^2)_{\text{edo}} = \frac{[\langle \tilde{v}_{\parallel}^2 \rangle]_{\text{edo}}}{[\langle \sigma_{\parallel}^2 \rangle]_{\text{edo}}} ; \quad (24)$$

must necessarily coincide, if deduced from observations, which is true also for the shape factors. Accordingly, the combination of Eqs. (22) and (23) yields:

$$(1 - \delta_C) \frac{(B_{\text{sel}})_{11}}{(B_{\text{sel}})_{33}} - 1 = \frac{(1 - \delta_B)(B_{\text{sel}})_{11}/(B_{\text{sel}})_{33} - 1}{\psi(1 - \delta_B)(B_{\text{sel}})_{11}/(B_{\text{sel}})_{33} + 1} ; \quad (25)$$

where the indices, C and B, denote anisotropy parameters related to the current and earlier (B05) attempt, respectively.

The values of the anisotropy parameter for sample objects, listed in Tab. 1, are taken from an earlier attempt (SX), where they have been determined in accordance with Eq. (23). For this reason, a comparison is needed between values of the rotation parameter, $(\chi_v^2)_C$ and $(\chi_v^2)_B$, defined by Eqs. (22) and (23), respectively. To this aim, the rotation parameter ratio:

$$\chi_{CB}^2 = \frac{(\chi_v^2)_C}{(\chi_v^2)_B} = \psi(1 - \delta_B) \frac{(B_{\text{sel}})_{11}}{(B_{\text{sel}})_{33}} + 1 ; \quad 0 < \epsilon_{31} < 1 ; \quad (26)$$

shall be considered, which is maximum for isotropic stress tensor, $\delta = 0$. In the spherical limit, $\epsilon_{31} = 1$, $(B_{\text{sel}})_{11} = (B_{\text{sel}})_{33}$, which implies $\delta = 0$, and Eq. (26) reduces to:

$$\chi_{\text{CB}}^2 = \psi + 1 \quad ; \quad \epsilon_{31} = 1 \quad ; \quad (27)$$

in the flat limit, $\epsilon_{31} = 0$, $(B_{\text{sel}})_{11} = \pi/2$, $(B_{\text{sel}})_{33} = 0$, which implies $\chi_{\text{CB}}^2 \rightarrow +\infty$ unless $\delta = 1$. In dealing with elliptical galaxies, $\epsilon_{31} \geq 0.3$, the flat limit is never attained. For realistic density profiles, numerical computations yield $\psi \approx 0.131$ in presence of flat rotation curves, $\overline{v_\phi} = \text{const}$ (B05), and $\psi \approx 0.15$ using Jeans models (SX).

The results are listed in Tab.3, where the values of the following parameters are calculated or deduced from Tab.1 for sample objects: the intrinsic meridional axis ratio, $\epsilon_{31} = 1 - \hat{e}$, Eq. (10); the shape factor ratio, $b_{23} = (B_{\text{sel}})_{22}/(B_{\text{sel}})_{33}$, Eq. (3b); the inclination angle, i , of the best fitting two-integral Jeans model (SIV); the anisotropy parameter, δ , determined from the solution of the dynamic models, supposed to be axisymmetric (SX); the sample object rotation parameter, $(\chi_v^2)_{\text{edo}} = [< \tilde{v}_{\parallel}^2 >]_{\text{edo}} / [< \sigma_{\parallel}^2 >]_{\text{edo}}$, Eqs. (11) and (12); the adjoint configuration rotation parameter, $(\chi_v^2)_C$, Eq. (22); the adjoint configuration rotation parameter, $(\chi_v^2)_B$, Eq. (23); the rotation parameter ratio, χ_{CB}^2 , Eq. (26); the ratio, $p = 1/(\sqrt{2}\chi_{\text{CB}})$; together with the kinematic classification, where F and S denote fast and slow rotators, respectively (SX). For sample objects with meridional axis ratio below the bifurcation point, $\epsilon_{31} < (\epsilon_{31})_{\text{bif}} = 0.582724$, the shape factors are determined for triaxial instead of axisymmetric configurations, where the minor equatorial axis is assumed to be parallel to the line of sight.

An inspection of Tab.3 shows that $\chi_{\text{CB}}^2 = 1.15\text{-}1.23$ and $1/(\sqrt{2}\chi_{\text{CB}}) = 0.64\text{-}0.66$. Curiously, the last range is consistent with the squared coefficient, 2×0.57^2 , of the best fitting relation between rotation parameters derived from integral-field and long-slit stellar kinematics (SX), the second expressed in terms of one-dimension peak velocity.

5 Discussion

Though the generalization of the ellipticity-rotation plane, $(O\hat{e}\chi_v^2)$, takes nonequilibrium figures into consideration, still galaxies may be thought of as fully virialized ($\zeta = 1$) unless a major merger is going on. On the other hand, cluster of galaxies are presently assembling and radial motions dominate at large clustercentric distances, which implies dynamical evolution ($\zeta \neq 1$). For this reason, only the sequence of equilibrium figures has been considered in dealing with elliptical galaxies. The rotation parameter, χ_v^2 , depends on the

Table 3: Comparison between intrinsic rotation parameters, $(\chi_v^2)_C$ and $(\chi_v^2)_B$, calculated for sample objects listed in Tab. 1, using Eqs. (22) and (23), respectively, for isotropic stress tensor ($\delta = 0$) and $\psi = 0.15$ (SX). Also listed are values of the ratios, $\chi_{CB}^2 = (\chi_v^2)_C/(\chi_v^2)_B$ and $p = 1/(\sqrt{2}\chi_{CB})$. The remaining parameters are taken or deduced from Tab. 1. For meridional axis ratios below the bifurcation point, $\epsilon_{31} < (\epsilon_{31})_{\text{bif}} = 0.582724$, the shape factors are determined for triaxial instead of axisymmetric configurations, where the minor equatorial axis is assumed to be parallel to the line of sight. Column captions: (1) NGC number; (2) intrinsic meridional axis ratio, $\epsilon_{31} = 1 - \hat{e}$, Eq. (10); (3) shape factor ratio, $b_{23} = (B_{\text{sel}})_{22}/(B_{\text{sel}})_{33}$, Eq. (3b); (4) inclination angle, i , of the best fitting two-integral Jeans model (SIV); (5) anisotropy parameter, δ , determined from the solution of the dynamic models, supposed to be axisymmetric (SX); (6) sample object rotation parameter, $(\chi_v^2)_{\text{edo}} = [\langle \tilde{v}_{\parallel}^2 \rangle]_{\text{edo}}/[\langle \sigma_{\parallel}^2 \rangle]_{\text{edo}}$, Eqs. (11) and (12); (7) adjoint configuration rotation parameter, $(\chi_v^2)_C$, Eq. (22); (8) adjoint configuration rotation parameter, $(\chi_v^2)_B$, Eq. (23); (9) rotation parameter ratio, χ_{CB}^2 , Eq. (26); (10) ratio, $p = 1/(\sqrt{2}\chi_{CB})$; (11) kinematic classification, where F and S denote fast and slow rotators, respectively (SX).

NGC	ϵ_{31}	b_{23}	i	δ	$(\chi_v^2)_{\text{edo}}$	$(\chi_v^2)_C$	$(\chi_v^2)_B$	χ_{CB}^2	p	KC
0821	0.60	1.53	90	0.20	0.07	0.35	0.29	1.23	0.64	F
2974	0.38	2.29	57	0.24	0.65	0.46	0.38	1.19	0.65	F
3377	0.54	1.68	90	0.25	0.24	0.38	0.31	1.22	0.64	F
3379	0.92	1.07	90	0.03	0.02	0.05	0.04	1.16	0.66	F
3608	0.82	1.18	90	0.13	0.00	0.12	0.10	1.18	0.65	S
4278	0.74	1.28	45	0.18	0.07	0.19	0.16	1.19	0.65	F
4374	0.85	1.14	90	0.08	0.00	0.09	0.08	1.17	0.65	S
4458	0.88	1.11	90	0.09	0.01	0.07	0.06	1.17	0.65	S
4473	0.54	1.68	73	0.34	0.05	0.38	0.31	1.22	0.64	F
4486	0.96	1.03	90	0.00	0.00	0.02	0.02	1.15	0.66	S
4552	0.96	1.03	90	0.02	0.00	0.02	0.02	1.15	0.66	S
4621	0.66	1.41	90	0.18	0.06	0.27	0.23	1.21	0.64	F
4660	0.47	1.89	70	0.30	0.26	0.40	0.33	1.21	0.64	F
5813	0.85	1.14	90	0.08	0.02	0.09	0.08	1.17	0.65	S
5845	0.65	1.43	90	0.15	0.13	0.29	0.24	1.21	0.64	F
5846	0.93	1.06	90	0.01	0.00	0.04	0.03	1.16	0.66	S

intrinsic squared mean equatorial tangential velocity component and velocity component dispersions, according to Eq. (5).

A different rotation parameter has been defined in an earlier attempt (B05), which depends on the sky-averaged mean streaming velocity parallel to the line of sight, the sky-averaged streaming velocity (parallel to the line of sight) dispersion, and the sky-averaged component velocity (parallel to the line of sight) dispersion related to nonstreaming motions.

The inclination angle, i , and the anisotropy parameter, δ , have been determined for sample objects by comparison with the dynamic models, under the assumption of axisymmetric configurations ($a_1 = a_2$), axisymmetric stress tensor ($\sigma_{11} = \sigma_{22}$), and flattened shapes ($a_1 > a_3$, $\sigma_{11} > \sigma_{33}$), as outlined in the parent paper (SX). On the other hand, it is shown in Fig. 2 that four sample objects are predicted to be triaxial as the ellipticity value related to the bifurcation point ($\hat{e}_{\text{bif}} = 0.417\,276$), marked by the vertical dotted line, is exceeded, and the most flattened configurations could be barlike (e.g., $\epsilon_{21} = 0.432\,232$ for $\epsilon_{31} = 0.345\,069$). Then some caution must be adopted in the interpretation of the triaxiality, especially for the most aspherical sample object (NGC 2974). To this respect, it is worth remembering that galaxies are embedded in dark (nonbaryonic) matter haloes, according to current cosmological scenarios.

The presence of a massive, embedding subsystem stabilizes the inner spheroid and shifts the bifurcation point (from axisymmetric to triaxial configurations) towards increasing ellipticities (Durisen 1978; Pacheco et al. 1986). In the special case of homogeneous subsystems, the bifurcation point is attained at $\hat{e} \approx 0.7$ for comparable masses within the volume of the inner spheroid (Caimmi 1996a), which can be considered as an upper limit. In fact, by comparison with the dynamic models, fast rotators appear to be axisymmetric while, paradoxically, slow rotators exhibit a moderate triaxiality (SX). Using triaxial dynamic models could provide better understanding on this point. An inspection of Fig. 2 and Tab. 1 shows that, for slow rotators (including NGC 3379) $0 \leq \hat{e} < 0.2$; $0 \leq \delta < 0.15$; $0 \leq \chi_v^2 < 0.15$; and for fast rotators (excluding NGC 3379) $0.2 \leq \hat{e} < 0.65$; $0.15 \leq \delta < 0.35$; $0.15 \leq \chi_v^2 < 0.5$; which could be an alternative kinematic classification with respect to earlier attempts (e.g., Emsellem et al. 2007). Richer samples should be dealt with to provide more conclusive evidence on this point.

If slow rotators (including NGC 3379) are nonrotating within the observational errors, and their shapes are elongated due to negative anisotropy parameters, $\delta < 0$ i.e. $\sigma_{11} = \sigma_{22} < \sigma_{33}$, a different kinematic classification is shown in Fig. 3 and Tab. 2. With regard to adjoint configurations with isotropic stress tensor, fast and slow rotators are affected by real and imaginary systematic rotation, respectively. It is, of course, a limiting situation,

in the sense that no zone of avoidance is expected on the sequence of adjoint configurations. If nonrotating elongated configurations really exist, slow rotators should be divided into two subclasses, namely (1) flattened in real rotation, and (2) elongated in imaginary rotation. In the latter alternative, elongated instead of flattened dynamic models should be used for determining the inclination angle and the anisotropy parameter by comparison with the data (SIV; SX), to gain consistency and to test the above interpretation.

Given a spherical galaxy with isotropic stress tensor, rotation (around a selected axis) kinetic energy may be added in infinite ways between two limiting situations, namely (a) systematic rotation, where circular motions are either clockwise or counterclockwise, and (b) random rotation, where the mean circular velocity is null. In any case, all the observables remain unchanged with the exception of the angular momentum and the stress tensor. More specifically, any system may be related to its adjoint configuration with isotropic stress tensor, without loss of generality, for ellipticity values above a threshold (Appendix B).

In this view, the elliptical side of the Hubble sequence may be interpreted as a sequence of equilibrium (adjoint) figures where the ellipticity, \hat{e} , is increasing with the rotation parameter, χ_v^2 . The original (elliptical side of the) Hubble sequence may be generalized on two respects, namely (1) from equilibrium ($\zeta = 1$) to nonequilibrium ($\zeta \neq 1$) figures, and (2) from real ($\hat{e} \geq 0$, $\chi_v^2 \geq 0$) to imaginary ($\hat{e} < 0$, $\chi_v^2 < 0$) rotation. More specifically, real rotation is related to flattened configurations and imaginary rotation to elongated configurations, spinning around the minor and the major axis, respectively.

The above classification is grounded on the assumption of homeoidally striated density profiles, regardless of the mechanism of formation. More specifically, configurations of equal shape related to different assembling processes belong to the same class. In reality, isophotes in elliptical galaxies may be boxy i.e. “overelliptic” or disky i.e. “underelliptic” where, in any case, the axis ratio changes with radius. This dichotomy, together with the one related to dwarf and giant elliptical galaxies, is interpreted as due to different past histories (e.g., Kormendy et al. 2009). On the other hand, a simplified description in terms of isophotes with constant axis ratio at all radii, implies a classification of equilibrium (or nonequilibrium with fixed virial index) figures which is independent of the formation and evolution processes.

6 Conclusion

The results of earlier investigations on homeoidally striated MacLaurin spheroids and Jacobi ellipsoids (CM05; Caimmi 2006a; C07) are used in the current attempt for the representation of nonequilibrium figures on the ellipticity-velocity plane, and of figures in imaginary rotation, where the effect is elongating instead of flattening, with respect to the rotation axis. The key concept is that the addition of kinetic energy related to tangential equatorial velocity components makes distorted boundaries regardless of what fraction translates in an increment of angular momentum, and what fraction in an increment of stress tensor equatorial components. Then any system admits an adjoint configuration with isotropic stress tensor, for ellipticity values above a threshold (Appendix B), and the related sequence can be considered without loss of generality. The kinetic energy is decomposed into contributions from cylindrical rotation, $E_{\text{rot}} = M(\overline{v_\phi})^2/2$, and tangential equatorial component velocity dispersion plus residual motions, $E_{\text{res}} = M(\sigma_{\phi\phi}^2 + \sigma_{ww}^2 + \sigma_{33}^2)/2$, and the rotation parameter is defined as $\chi_v^2 = E_{\text{rot}}/E_{\text{res}}$.

Elliptical galaxies are idealized as homeoidally striated MacLaurin spheroids and Jacobi ellipsoids, and their position on the ellipticity-velocity plane is inferred from observations related to a sample (CV08, $N = 16$) extracted from richer samples of early-type galaxies investigated within the SAURON project (SIV, $N = 25$; SX, $N = 48$). The location of model galaxies on the $(\mathcal{O}\hat{e}\chi_v^2)$ plane is determined through the following steps (C09): (i) select SAURON data of interest; (ii) calculate the parameters appearing in the virial equations; (iii) make a correspondence between model galaxies and sample objects; (iv) represent model galaxies on the $(\mathcal{O}\hat{e}\chi_v^2)$ plane.

The main results found in the present investigation may be summarized as follows.

- (1) Sequences of homeoidally striated MacLaurin spheroids and Jacobi ellipsoids with isotropic stress tensor are defined and plotted on the $(\mathcal{O}\hat{e}\chi_v^2)$ plane, without loss of generality: for any system with anisotropic stress tensor an adjoint configuration exists, with isotropic stress tensor and remaining parameters unchanged with the exception of the angular momentum, for ellipticity values above a threshold.
- (2) Sequences of homeoidally striated MacLaurin spheroids and Jacobi ellipsoids are generalized to nonequilibrium figures.
- (3) Sequences of homeoidally striated MacLaurin spheroids and Jacobi ellipsoids are generalized to imaginary rotation which acts in elongating, instead of flattening, with respect to the rotation axis.

- (4) An alternative kinematic classification with respect to earlier attempts (e.g., Emsellem et al. 2007) is proposed, where slow rotators are characterized by low ellipticities ($0 \leq \hat{e} < 0.2$), low anisotropy parameters ($0 \leq \delta < 0.15$), and low rotation parameters ($0 \leq \chi_v^2 < 0.15$), and fast rotators by large ellipticities ($0.2 \leq \hat{e} < 0.65$), large anisotropy parameters ($0.15 \leq \delta < 0.35$), and large rotation parameters ($0.15 \leq \chi_v^2 < 0.5$). Richer samples should be used to test the validity of the above interpretation.
- (5) A possible interpretation of slow rotators as nonrotating and elongated due to a negative anisotropy parameter, instead of flattened due to a positive anisotropy parameter, is exploited.
- (6) The elliptical side of the Hubble morphological sequence is interpreted as a sequence of equilibrium (adjoint) figures where the ellipticity is an increasing function of the rotation parameter. Accordingly, slow rotators correspond to early classes (E0-E2 in the oblate limit and E-2-E0 in the prolate limit) and fast rotators to late classes (E3-E6). In this view, boundaries are rotationally distorted regardless of what fraction of tangential equatorial velocity components is related to angular momentum, and what fraction to stress tensor equatorial components.

7 Acknowledgements

Thanks are due to T. Valentinuzzi for fruitful discussions.

References

- [1] Bacon, R., et al.: 2002, in Bergeron J., Monnet G., eds., Scientific Drivers for ESO Future VLT/VLTI Instrumentation, Springer, Berlin, p. 108.
- [2] Bailin, J., Steinmetz, M.: 2004, *Astrophys. J.*, 616, 27.
- [3] Bertola, F., Capaccioli, M.: 1975, *Astrophys. J.*, 200, 439.
- [4] Binney, J.: 1976, *Mon. Not. R. Astron. Soc.*, 177, 19.
- [5] Binney, J.: 1978, *Mon. Not. R. Astron. Soc.*, 183, 501.
- [6] Binney, J.: 1980, *Mon. Not. R. Astron. Soc.*, 190, 421.
- [7] Binney, J.: 2005, *Mon. Not. R. Astron. Soc.*, 363, 937. (B05)

- [8] Binney, J., Tremaine, S., 1987. *Galactic Dynamics*, Princeton University Press, Princeton.
- [9] Caimmi, R.: 1980, *Astrphys. Space Sci.*, 71, 75.
- [10] Caimmi, R.: 1983, *Astrphys. Space Sci.*, 93, 403.
- [11] Caimmi, R.: 1992, *Astron. Nachr.*, 313, 165.
- [12] Caimmi, R.: 1996a, *Acta Cosmologica*, XXII, 21.
- [13] Caimmi, R.: 1996b, *Astron. Nachr.*, 317, 401.
- [14] Caimmi, R.: 2006a, *Astron. Nachr.*, 327, 925.
- [15] Caimmi, R.: 2006b, *Serb. Astron. J.*, 173, 13.
- [16] Caimmi, R.: 2007, *Serb. Astron. J.*, 174, 13. (C07)
- [17] Caimmi, R.: 2008, *Serb. Astron. J.*, 176, 23. (C08)
- [18] Caimmi, R.: 2009a, *New Astron.*, 14, 254.
- [19] Caimmi, R.: 2009b, arxiv 0907.1018. (C09)
- [20] Caimmi, R., Marmo, C.: 2005, *Astron. Nachr.*, 326, 465. (CM05)
- [21] Caimmi, R., Valentinuzzi, T.: 2008, *Serb. Astron. J.*, 177, 15. (CV08)
- [22] Cappellari, M., Bacon, R., Bureau, M., et al.: 2006, *Mon. Not. R. Astron. Soc.*, 366, 1126. (SIV)
- [23] Cappellari, M., Emsellem, E., Bacon, R., et al.: 2007, *Mon. Not. R. Astron. Soc.*, 379, 418. (SX)
- [24] de Zeeuw, T., et al.: 2002, *Mon. Not. R. Astron. Soc.*, 329, 513.
- [25] Durisen, R.H.: 1978, *Astrophys.J.*, 224, 826.
- [26] Emsellem, E., et al.: 2007, *Mon. Not. R. Astron. Soc.*, 379, 401.
- [27] Hoeft, M., Mucket, J.P., Gottlöber, S.: 2004, *Astrophys. J.*, 602, 162.
- [28] Hubble, E.P.: 1926, *Astrophys. J.*, 64, 321.
- [29] Illingworth, G.: 1977, *Astrophys. J.*, 218, L43.

- [30] Illingworth, G.: 1981, in S.M. Fall and D. Lynden-Bell (eds.), *Structure and Evolution of Normal Galaxies*, Cambridge University Press, p.27.
- [31] Jeans, J.: 1929, *Astronomy and Cosmogony*, Dover Publications, New York, 1961.
- [32] Kelz, A., Roth, M.M., Becker, T.: 2003, *SPIE*, 4841, 1057.
- [33] Kormendy, J., Fisher, D.B., Cornell, M.E., Bender, R.: 2009, *Astrophys. J. Supp. Ser.*, 182, 216.
- [34] Lai, D., Rasio, F.A., Shapiro, S.L.: 1993, *Astrophys. J. Supp.*, 88, 205.
- [35] Lynden-Bell, D.: 1960, *Mon. Not. R. Astron. Soc.*, 120, 204.
- [36] Lynden-Bell, D.: 1962, *Mon. Not. R. Astron. Soc.*, 124, 1.
- [37] Meza, A.: 2002, *Astron. Astrophys.*, 395, 25.
- [38] Pacheco, F., Pucacco, G., Ruffini, R.: 1986, *Astron. Astrophys.*, 161, 39.
- [39] Rasia, E., Tormen, G., Moscardini, L.: 2004, *Mon. Not. R. Astron. Soc.*, 351, 237.
- [40] Roberts, P.H.: 1962, *Astrophys. J.*, 136, 1108.
- [41] Schechter, P.L., Gunn, J.E.: 1979, *Astrophys. J.*, 229, 472.
- [42] Vandervoort, P.O.: 1980a, *Astrophys. J.*, 240, 478.
- [43] Vandervoort, P.O.: 1980b, *Astrophys. J.*, 241, 316.
- [44] Vandervoort, P.O.: 1982, *Astrophys. J.*, 256, L41.
- [45] Vandervoort, P.O., Welty, D.E.: 1981, *Astrophys. J.*, 248, 504.

Appendix

A Rotation and residual kinetic energy

With regard to a generic matter distribution, let $(Ox_1x_2x_3)$ be a reference frame where the origin coincides with the centre of mass, and the coordinate axis, x_3 , coincides with the rotation axis. Let $v_\phi(x_1, x_2, x_3, t)$ be the tangential equatorial (with respect to the rotation axis) velocity component,

related to the generic particle at the point, $P(x_1, x_2, x_3)$, at the time, t . The corresponding angular velocity is defined by the relation:

$$v_\phi(x_1, x_2, x_3, t) = \Omega(x_1, x_2, x_3, t)w \quad ; \quad w^2 = x_1^2 + x_2^2 \quad ; \quad (28)$$

which can also be extended to mean values, $\overline{v_\phi}(x_1, x_2, x_3, t)$, $\overline{\Omega}(x_1, x_2, x_3, t)$, within an infinitesimal volume element, $dx_1 dx_2 dx_3$, placed at the same point, P . In the following relations, the time dependence shall be omitted on the quantities at the left-hand side, to gain simplicity.

The mass-weighted tangential equatorial velocity component and squared tangential equatorial velocity component read:

$$\overline{v_\phi} = \frac{1}{M} \int \int \int \overline{v_\phi}(x_1, x_2, x_3, t) \rho(x_1, x_2, x_3, t) dx_1 dx_2 dx_3 \quad ; \quad (29)$$

$$\overline{(v_\phi^2)} = \frac{1}{M} \int \int \int \overline{v_\phi^2}(x_1, x_2, x_3, t) \rho(x_1, x_2, x_3, t) dx_1 dx_2 dx_3 \quad ; \quad (30)$$

where M is the total mass and ρ the local density. The empirical variance is:

$$\sigma_{\phi\phi}^2 = \overline{(v_\phi^2)} - (\overline{v_\phi})^2 \quad ; \quad (31)$$

by definition.

The moment-of-inertia-weighted angular velocity and squared angular velocity read:

$$\overline{\Omega} = \frac{1}{I_3} \int \int \int \overline{\Omega}(x_1, x_2, x_3, t) w^2 \rho(x_1, x_2, x_3, t) dx_1 dx_2 dx_3 \quad ; \quad (32)$$

$$\overline{(\Omega^2)} = \frac{1}{I_3} \int \int \int \overline{\Omega^2}(x_1, x_2, x_3, t) w^2 \rho(x_1, x_2, x_3, t) dx_1 dx_2 dx_3 \quad ; \quad (33)$$

where I_3 is the moment of inertia with respect to the rotation axis, x_3 . The empirical variance is:

$$\sigma_{\Omega\Omega}^2 = \overline{(\Omega^2)} - (\overline{\Omega})^2 \quad ; \quad (34)$$

by definition.

A link between mass and moment of inertia is provided by the following relation:

$$R_{G3}^2 = \frac{I_3}{M} = \frac{1}{M} \int \int \int w^2 \rho(x_1, x_2, x_3, t) dx_1 dx_2 dx_3 \quad ; \quad (35)$$

where R_{G3} is the radius of gyration with respect to the rotation axis, x_3 . Using Eqs. (28) and (35), the combination of Eqs. (30), (31), (33), and (34) yields:

$$\overline{(v_\phi^2)} = \overline{(\Omega^2)} R_{G3}^2 \quad ; \quad (36)$$

$$(\overline{v_\phi})^2 + \sigma_{\phi\phi}^2 = [(\overline{\Omega})^2 + \sigma_{\Omega\Omega}^2] R_{G3}^2 \quad ; \quad (37)$$

while, on the other hand, $\overline{v_\phi} \neq \overline{\Omega} R_{G3}$, $\sigma_{\phi\phi} \neq \sigma_{\Omega\Omega} R_{G3}$, and a different averaging is needed on either v_ϕ or Ω .

To this aim, the (MR_{G3}) -weighted circular velocity, $\overline{v_\Omega}$, and the (MR_{G3}) -weighted angular velocity, $\overline{\Omega_v}$, are defined as:

$$\overline{v_\Omega} = \overline{\Omega} R_{G3} = \frac{R_{G3}}{I_3} \int \int \int \overline{v_\phi}(x_1, x_2, x_3, t) w \rho(x_1, x_2, x_3, t) dx_1 dx_2 dx_3; \quad (38)$$

$$\overline{\Omega_v} = \frac{\overline{v_\phi}}{R_{G3}} = \frac{R_{G3}}{I_3} \int \int \int \overline{\Omega}(x_1, x_2, x_3, t) w \rho(x_1, x_2, x_3, t) dx_1 dx_2 dx_3; \quad (39)$$

and the angular momentum with respect to the rotation axis, x_3 , is defined by the integral on the right-hand side of Eq. (32) or (38), which yields:

$$J_3 = I_3 \overline{\Omega} = M \overline{v_\Omega} R_{G3} \quad ; \quad (40)$$

in terms of the moment-of-inertia-weighted angular velocity and the (MR_{G3}) -weighted circular velocity, respectively.

The combination of Eqs. (35), (36), (38), and (39) yields the following expression for the radius of gyration:

$$R_{G3}^2 = \frac{I_3}{M} = \frac{\overline{(v_\phi^2)}}{(\overline{\Omega^2})} = \frac{(\overline{v_\Omega})^2}{(\overline{\Omega})^2} = \frac{(\overline{v_\phi})^2}{(\overline{\Omega_v})^2} \quad ; \quad (41)$$

where the differences, $\overline{(v_\phi^2)} - (\overline{v_\Omega})^2$, $\overline{(\Omega^2)} - (\overline{\Omega_v})^2$, cannot be related to empirical variances as the corresponding terms are weighted in different ways.

Accordingly, the rotation kinetic energy related to tangential equatorial velocity components may be expressed as:

$$(E_{\text{kin}})_{\phi\phi} = \frac{1}{2} M \left[(\overline{v_\phi})^2 + \sigma_{\phi\phi}^2 \right] = E_{\text{rot}} + \frac{1}{2} M \sigma_{\phi\phi}^2 \quad ; \quad (42a)$$

$$E_{\text{rot}} = \frac{1}{2} M (\overline{v_\phi})^2 \quad ; \quad (42b)$$

and the total kinetic energy reads:

$$E_{\text{kin}} = E_{\text{rot}} + E_{\text{res}} \quad ; \quad (43a)$$

$$E_{\text{res}} = \frac{1}{2} M \left[\overline{(v_w^2)} + \overline{(v_3^2)} + \sigma_{\phi\phi}^2 \right] \quad ; \quad (43b)$$

$$\overline{(v_w^2)} = (\overline{v_w})^2 + \sigma_{ww}^2 = \sigma_{ww}^2 \quad ; \quad (43c)$$

$$\overline{(v_3^2)} = (\overline{v_3})^2 + \sigma_{33}^2 = \sigma_{33}^2 \quad ; \quad (43d)$$

where v_w and v_3 are the radial equatorial and polar velocity components and $\overline{v_w} = \overline{v_3} = 0$ provided the centre of mass coincides with the origin of the

coordinates (for further details refer to e.g., C07). Accordingly, Eq. (43b) reduces to:

$$E_{\text{res}} = \frac{1}{2}M\sigma^2 = \frac{1}{2}M \left(\sigma_{\phi\phi}^2 + \sigma_{ww}^2 + \sigma_{33}^2 \right) ; \quad (44)$$

which is equivalent to:

$$E_{\text{res}} = \frac{1}{2}M\sigma^2 = \frac{1}{2}M \left(\sigma_{11}^2 + \sigma_{22}^2 + \sigma_{33}^2 \right) ; \quad (45)$$

in Cartesian coordinates.

B Systematic and random rotation excess

Let two matter distributions be characterized by equal density profiles and shapes, but isotropic and anisotropic stress tensor, respectively, and different amount of angular momentum. The generalized virial equations, Eqs. (1), read:

$$2[(E_{\text{rot}})_{pp}]_{\text{ani}} + 2[(\tilde{E}_{\text{res}})_{pp}]_{\text{ani}} + (E_{\text{pot}})_{pp} = 0 ; \quad p = 1, 2, 3 ; \quad (46a)$$

$$2[(E_{\text{rot}})_{pp}]_{\text{iso}} + 2[(\tilde{E}_{\text{res}})_{pp}]_{\text{iso}} + (E_{\text{pot}})_{pp} = 0 ; \quad p = 1, 2, 3 ; \quad (46b)$$

$$(E_{\text{rot}})_{11} + (E_{\text{rot}})_{22} = E_{\text{rot}} ; \quad (E_{\text{rot}})_{33} = 0 ; \quad (46c)$$

where $(\tilde{E}_{\text{res}})_{pp} = \zeta_{pp}E_{\text{res}}$ is the residual kinetic-energy tensor of the related equilibrium figure.

In both cases, the potential-energy tensor remains unchanged, which implies the following relation:

$$[(\tilde{E}_{\text{res}})_{33}]_{\text{ani}} = [(\tilde{E}_{\text{res}})_{pp}]_{\text{iso}} ; \quad p = 1, 2, 3 ; \quad (47)$$

and the substitution of Eq. (47) into (46) yields:

$$\begin{aligned} & [(E_{\text{rot}})_{qq}]_{\text{iso}} + \Delta(E_{\text{rot}})_{qq} + [(\tilde{E}_{\text{res}})_{qq}]_{\text{iso}} + \Delta(\tilde{E}_{\text{res}})_{qq} \\ & = [(E_{\text{rot}})_{qq}]_{\text{iso}} + [(\tilde{E}_{\text{res}})_{qq}]_{\text{iso}} ; \quad q = 1, 2 ; \end{aligned} \quad (48a)$$

$$\Delta(E_{\text{rot}})_{qq} = [(E_{\text{rot}})_{qq}]_{\text{ani}} - [(E_{\text{rot}})_{qq}]_{\text{iso}} ; \quad (48b)$$

$$\Delta(\tilde{E}_{\text{res}})_{qq} = [(\tilde{E}_{\text{res}})_{qq}]_{\text{ani}} - [(\tilde{E}_{\text{res}})_{qq}]_{\text{iso}} ; \quad (48c)$$

which is equivalent to:

$$\Delta(E_{\text{rot}})_{qq} + \Delta(\tilde{E}_{\text{res}})_{qq} = 0 ; \quad (49)$$

where the first and the second term of the sum may be conceived as a (positive or negative) systematic and random rotation excess, respectively. Random

rotation has to be intended as related to a selected axis, with a null mean value.

With regard to nonequilibrium figures, the validity of the relation:

$$\Delta(E_{\text{rot}})_{qq} + \Delta(E_{\text{res}})_{qq} = 0 \quad ; \quad (50)$$

means that a fixed amount of rotation energy has been converted into residual energy (or vice versa). The combination of Eqs. (49) and (50) yields:

$$\Delta(E_{\text{res}})_{qq} = \Delta(\tilde{E}_{\text{res}})_{qq} \quad ; \quad (51)$$

and Eq. (50) may be cast under the explicit form:

$$\Delta[(\overline{v_\phi})_{qq}]^2 + \Delta(\sigma_{qq}^2) = 0 \quad ; \quad (52)$$

according to Eqs. (42) and (43). The above results may be reduced to a single statement.

Theorem *Given a matter distribution with assigned density profile, shape, virial index, $\zeta = \tilde{E}_{\text{res}}/E_{\text{res}}$, and isotropic stress tensor, an infinity of adjoint configurations with anisotropic stress tensor exist, for which the sum of systematic and random rotation excess is null.*

According to earlier attempts (Lynden-Bell 1960, 1962; Meza 2002) the distribution function is independent of the sign of the tangential velocity components, and the whole set of possible configurations is characterized by an equal amount of both kinetic and potential energy. In other words, clockwise and counterclockwise circular motions are indistinguishable to this respect, passing from systematic (maximal squared mean tangential equatorial velocity component) to random (minimal squared mean tangential equatorial velocity component) rotation. An anisotropic stress tensor could be due to the prevalence of either systematic rotation ($\sigma_{11} = \sigma_{22} < \sigma_{33}$) or random rotation ($\sigma_{11} = \sigma_{22} > \sigma_{33}$) with respect to the adjoint configuration with isotropic stress tensor.

In the limiting case of flat configurations, $\epsilon_{31} \rightarrow 0$, $(E_{\text{pot}})_{33} \rightarrow 0$ (e.g., Caimmi 2009a), Eq. (1b) implies $(E_{\text{res}})_{33} = \zeta_{33} E_{\text{res}} \rightarrow 0$ and $(E_{\text{res}})_{qq} \rightarrow 0$ for isotropic stress tensor. In other words, flat configurations with isotropic stress tensor must necessarily be self-gravitating. Rotation curves depend on density profiles, ranging from linear curves related to homogeneous systems to Keplerian curves related to Roche systems. Accordingly, $\sigma_{\phi\phi} = 0$ in the former alternative, growing up to a maximum, $\sigma_{\phi\phi} > 0$, in the latter. But $\sigma_{\phi\phi} > 0$ would imply $(E_{\text{res}})_{qq} > 0$, which is in contradiction with either sufficiently flattened configurations or isotropic stress tensors. Then a threshold in meridional axis ratio exists, $\epsilon_{31} = \epsilon_{31}^*$, below which configurations with isotropic stress tensor cannot exist for an assigned density profile.

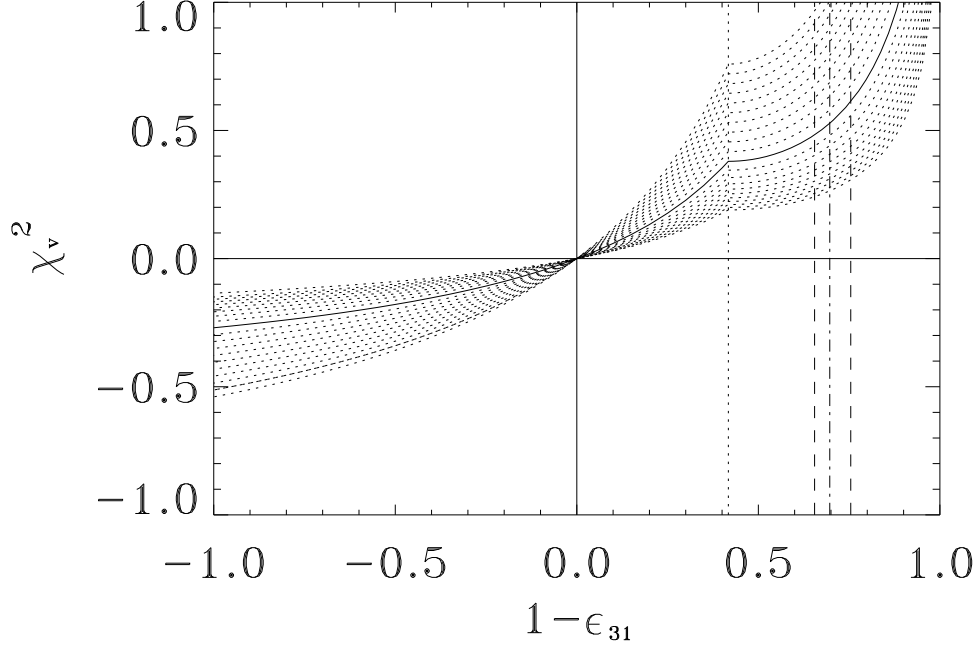


Figure 1: The rotation parameter, χ_v^2 , as a function of the meridional ellipticity, $\hat{e} = 1 - \epsilon_{31}$, for sequences of equilibrium (full) and nonequilibrium (dotted) figures with isotropic stress tensor. For equilibrium figures, $\zeta = \tilde{E}_{\text{res}}/E_{\text{res}} = 1$. For nonequilibrium figures, $\zeta = 1.1, 1.2, \dots, 2.0$ (above the equilibrium sequence on the first quadrant), and $\zeta = 1/1.1, 1/1.2, \dots, 1/2.0$ (below the equilibrium sequence on the first quadrant). Configurations lying on the first and third quadrant are in real and imaginary rotation, respectively. Nonrotating configurations are placed at the origin. Caption of vertical lines: dotted - bifurcation from axisymmetric to triaxial configurations; dashed - bifurcation from triaxial (left) and axisymmetric (right) to pear-shaped configurations; dot-dashed - onset of dynamical instability in axisymmetric configurations.

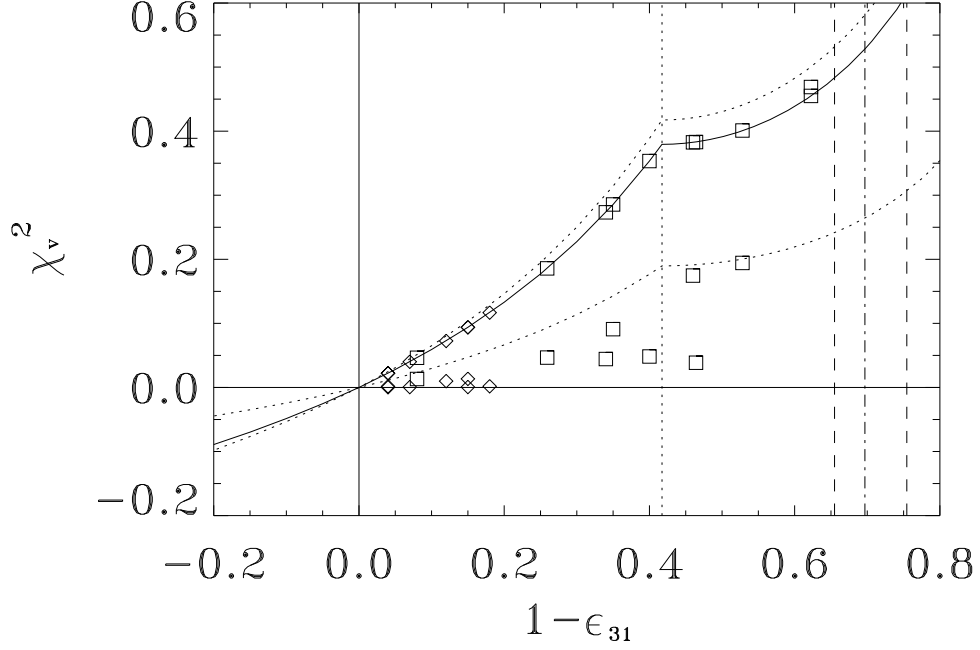


Figure 2: Position of elliptical galaxies listed in Tab. 1, on the $(O\hat{e}\chi_v^2)$ plane, denoted as squares and diamonds for fast and slow rotators, respectively. Curves are taken from Fig. 1, related to equilibrium figures ($\zeta = 1$, full line) and nonequilibrium figures ($\zeta = 1.1$, up on the first quadrant; $\zeta = 0.5$, down on the first quadrant; dotted lines) with isotropic stress tensor. Caption of vertical lines as in Fig. 1. The adjoint configurations with isotropic stress tensor and equal shape, are also positioned on the sequence of equilibrium figures using the same symbols, as the result of a vertical shift. A similar procedure holds, in general, for an assigned sequence of nonequilibrium figures with isotropic stress tensor.

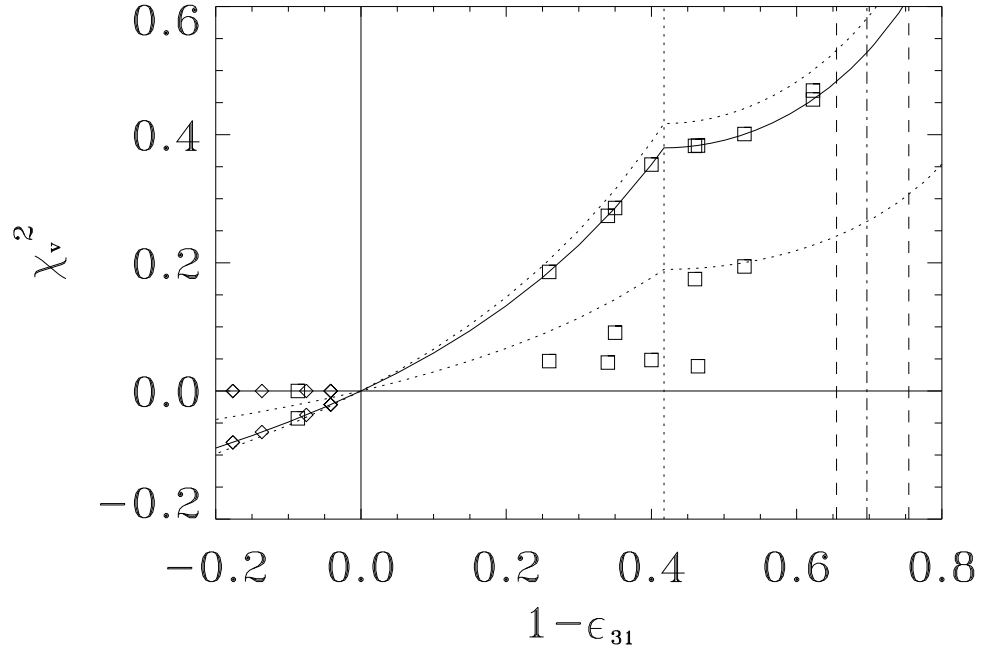


Figure 3: Same as in Fig. 2, but under the assumption that slow rotators (NGC 3379 included) are nonrotating within the observational errors and elongated due to an anisotropic stress tensor. For further details refer to the text. Captions as in Fig. 2.